INTERNATIONAL JOURNAL FOR NUMERICAL METHODS IN FLUIDS
*Int. J. Numer. Meth. Fluids* 2009; **60**:1011–1031
Published online 17 October 2008 in Wiley InterScience (www.interscience.wiley.com). DOI: 10.1002/fld.1929

# Linear Galerkin vs mixed finite element 2D flow fields

Mario Putti[1] and Flavio Sartoretto[2,*,†]

[1]*Dipartimento di Metodi e Modelli Matematici per le Scienze Applicate, Università di Padova, Italy*
[2]*Dipartimento di Informatica, Università di Venezia, via Torino 155, Mestre VE 30173, Italy*

## SUMMARY

Numerical velocity fields arising from the solution of diffusion equations by the finite element (FE) and the mixed hybrid finite element (MHFE) schemes display different behaviors. In this paper we analyze the characteristics of the two different velocity fields in terms of both accuracy and mass balance properties. General theoretical findings are mostly concerned with the asymptotic behavior of the numerical schemes, i.e. they look at properties as the mesh size tends to zero. For practical applications, it is necessary to work with a fixed mesh of given size. Thus, we attempt to characterize the numerical flow field accuracy by analyzing the resulting mass balance characteristics on a fixed mesh. The comparison is carried out by using direct local mass balance evaluations and by calculating streamlines. We detail the important differences, advantages, and disadvantages of the two approaches. In particular, we show that both FE and MH are perfectly conservative (up to the residual of the linear system solution) if proper control volumes are used. MH streamlines are admissible, i.e. numerical normal fluxes across cell interfaces are continuous. Since continuity of the normal fluxes is not guaranteed by FE, the resulting streamlines are less accurate. Copyright © 2008 John Wiley & Sons, Ltd.

Received 19 September 2007; Revised 19 August 2008; Accepted 21 August 2008

KEY WORDS: finite elements; mixed finite elements; velocity field; mass balance; potential flow; Voronoi tessellation

## 1. INTRODUCTION

We consider the classical steady-state diffusion equation governing potential flow in two-dimensional domains. This equation generally describes conservation of mass or energy fluxes, and is often used to calculate velocity fields. When used to represent convective flux in a

---

*Correspondence to: Flavio Sartoretto, Dipartimento di Informatica, Università di Venezia, via Torino 155, Mestre VE 30173, Italy.
†E-mail: sartoret@dsi.unive.it

Contract/grant sponsor: Italian MIUR-PRIN 2004 Project
Contract/grant sponsor: University of Padova Progetto di Ateneo 2004

convection–diffusion equation, the velocity field **v** must be 'conservative' or 'divergence free', if mass balance of the convected quantity needs to be conserved [1].

The problem of fulfilling the conservation properties of a numerical flow field has been addressed in a number of works [2–5]. It is often reported that Galerkin finite element (FE) approaches lead to inaccurate and non-conservative velocity fields [6–8]. In other words, though theory guarantees optimal convergence, there are instances when local errors may be large not due to lack of convergence, which may occur in highly anisotropic problems because of the mesh locking phenomenon [9], but due to a large asymptotic error constant. This problem is often tackled by post processing the numerical velocities [2]. For example, in [8], the author approximates the velocity vector components by means of the same linear basis functions used in the discretization of the conservation equation, and then imposes a weak form of the momentum equation (Darcy's law in this case). The resulting velocity fields are mass conservative, but suffer from severe loss of accuracy when the diffusion coefficient $K$ changes in space. For two-dimensional triangulations, [3] enforce an irrotational field on local patches, so that a divergence-free velocity can be recovered, but this technique is not extensible to three spatial dimensions. Being based on post processing of the velocities, all these approaches are not completely satisfactory, in the sense that the resulting field is changed by the post-processing method, and may not accurately resolve the original mass balance equation. As an alternative, the mixed FE (MFE) and the equivalent mixed hybrid (MH) FE techniques have been proposed to address the problem of non-conservative velocity fields [10–13]. In large-scale applications, computational efficiency suggests to exploit the lowest-order RT0-P0 (zero order [11]) formulation, which is the most commonly used approach, for examples in porous media flow.

When working on unstructured triangular meshes, numerical approximations of the velocity **v** obtained from linear Galerkin FE-P1 solutions of the conservation equation are usually piecewise continuous functions that should satisfy the divergence-free property. We note here that the FE-P1 on Delaunay meshes is equivalent to the finite volume (FV) or, more conveniently, to the orthogonal sub-domain collocation (OSC) method on Voronoi cells [7, 14, 15]. On triangular meshes, however, the divergence-free property is not satisfied by the velocity fields coming from FE-P1 [6, 16]. On the other hand, velocity fields arising from the RT0-P0 MFE or MH are always conservative [12]. For this reason, RT0-P0, which can be considered closely related to either cell-centered finite volumes on triangles or integrated finite differences on quadrilaterals [4, 5, 17–20], is often preferred to FE-P1 for the numerical solution of the mass balance equation, even though RT0-P0 is in general computationally less convenient than FE-P1. In fact, the linear system arising from RT0-P0, in its hybrid implementation, has on the average a larger number of unknowns with respect to FE-P1 (by a factor about 2.5 in 2D problems, and more than 7–10 in 3D problems). Moreover, RT0-P0 seems to be numerically less robust than FE-P1 when dealing with unstructured triangular meshes and/or heterogeneous, anisotropic media [21].

Theoretical findings for **v** show that both FE and MH yield optimal convergence rates, provided the usual regularity constraints on the mesh angles and on the smoothness of the solution are fulfilled. For example, both FE-P1 and RT0-P0 achieve first-order convergence for the solution gradients [13] (see also Section 2.2 in the sequel). This result suggests that the differences between the FE-P1 and RT0-P0 velocity fields cannot be too large, at least close to the asymptotic regime. On the other hand, numerical experiments carried out on a fixed mesh show important differences in the discrete gradient fields, and these differences are the subject of our interest in this study.

When working on real problems one is not concerned with the asymptotic case, since in most situations the number of elements that ensures the inception of this regime is prohibitively large.

It is thus important to understand the behavior of the different discretization strategies for a given mesh. This problem is however difficult to study because of a lack of appropriate tools for a quantitative comparison between different numerical solutions, and in particular different numerical flow fields. In other words, there is no standard way for measuring the accuracy of numerically calculated gradients at a fixed mesh size. Formal *a posteriori* error estimates are generally written as a function of appropriate norms of the real solution and its gradient. In the cases of practical interest, the gradient of the real solution often displays discontinuities that make these estimates less useful for determining the numerical solution accuracy, albeit they obviously remain of fundamental importance in grid refinement techniques. Thus, we look at *a posteriori* characteristics of the true solution, which are satisfied by the numerical solution and use these properties to characterize its accuracy and to highlight situations when one scheme outperforms the other. We concentrate our efforts on FE-P1 and RT0-P0 as they are two standard approaches and are among the most popular methods for solving diffusion equations. We look mainly at the local mass conservation properties. This task is pursued by first looking at mass flux balance in different control volumes, and then successively analyzing the steady-state trajectories resulting from particle tracking integration of the numerical flow field. We find that both schemes are equally mass conservative, contrary to general belief, if the proper control volumes are considered. On the other hand, our results show that the streamlines obtained from the two numerical vector fields are drastically different, showing that the generating vector fields are different. We try to give an explanation of this phenomenon and to propose research directions that may lead to a better understanding of these problems.

We consider the linear Galerkin FE and the RT0-P0 MHFE implementations on two-dimensional unstructured triangulations with constant and heterogeneous scalar coefficients. Note that, RT0-P0 is a standard approach described by many authors (see, e.g. [11, 13, 22]). It is used in many applications, as an example in porous media flow [12, 23, 24]. The importance of the problems, we deal with in this paper, is testified by many recent proposals for new techniques founded on homological theory (see e.g. [25]). On the other hand, we feel it is important to understand the details of the most commonly used methods and to resolve misconceptions and doubts that in particular pervade certain engineering literature. It is also important to observe that the proposed comparison relies heavily on the equivalence between the Linear Galerkin FE on Delaunay meshes and OSC on Voronoi cells. Unfortunately, this equivalence neither hold in three spatial dimensions [7, 26], nor for higher-order FE basis functions. It is beyond the scope of this study to investigate the behavior of such schemes.

## 2. NUMERICAL DISCRETIZATIONS

The transient diffusion equation in a domain $\Omega \in \mathbb{R}^2$, governing for example saturated porous media flow, can be written as:

$$\begin{aligned} \operatorname{div} \mathbf{v} &= f \\ (x, y) &\in \Omega \end{aligned} \tag{1}$$

$$\mathbf{v} = -K \nabla p \tag{2}$$

where $p$ is the pressure head (potential), $\mathbf{v}$ is the velocity vector, $K$ is the diffusion (or hydraulic conductivity) coefficient, here assumed a strictly positive scalar function, and $f$ is a source or

DOI: 10.1002/fld

sink term. Dirichlet or Neumann boundary conditions must be given to identify a well-posed mathematical formulation, $p(x,y)=\bar{p}(x,y)$ on $\Gamma_{\mathrm{D}}$, $\mathbf{v}\cdot\mathbf{n}=\bar{q}(x,y)$ on $\Gamma_{\mathrm{N}}$, where $\bar{p}$ is the prescribed pressure head (Dirichlet conditions) on the boundary portion $\Gamma_{\mathrm{D}}$, the vector $\mathbf{n}$ is the outward normal unit vector, and $\bar{q}$ is the prescribed Neumann flux across the boundary portion $\Gamma_{\mathrm{N}}$. The boundary segments satisfy $\Gamma_{\mathrm{D}}\cup\Gamma_{\mathrm{N}}=\partial\Omega$. In the interior of the domain we allow the diffusion coefficient $K$ to vary abruptly, as is typical, e.g. in groundwater flow problems. At the interfaces where $K$ changes, which are supposed to be sufficiently smooth, the analytical solution is continuous as well as the flux normal to the interface, but gradient discontinuities occur.

Let the domain $\Omega$ be discretized by a triangular two-dimensional mesh $\mathscr{T}=\bigcup_{t=1}^{M}T_t$, characterized by $N$ nodes, $M$ triangles, and $E$ edges or sides. The diffusion coefficient, $K$, is discretized by assuming that $K=K_t$ is constant on any mesh triangle.

### 2.1. Galerkin P1 FE discretization

The FE-P1 method considered in this article is a standard Galerkin approach that uses piecewise linear basis functions to approximate the unknown $p(x,y)$ of (2) by:

$$p(x,y)\approx p^{(\mathrm{FE})}=\sum_{i=1}^{N}p_i\xi_i(x,y)$$

where $\xi_i(x,y)$ is the classical roof function on node $N_i$, and $p_i$ is the corresponding nodal pressure value. Application of the usual Galerkin procedure results in a symmetric positive definite linear system for the unknown vector $\mathbf{p}=\{p_i\}$, whose size equals the number of nodes. The discrete velocity on triangle $T_t$ is proportional to the gradient of the pressure, which is constant over $T_t$. The numerical velocity field is thus a piecewise constant function, given by

$$\mathbf{v}^{(\mathrm{FE})}(x,y)=\sum_{t=1}^{M}\mathbf{v}_t^{(\mathrm{FE})}\chi_t(x,y),\quad \mathbf{v}_t^{(\mathrm{FE})}=-\sum_{j=1}^{3}K_t\nabla\xi_{j,t}(x,y)p_j \tag{3}$$

where $\nabla\xi_{j,t}(x,y)$ is the (constant) gradient of the piecewise linear basis function $\xi_j$ restricted to triangle $T_t$. The index $j$ denotes the $j$th vertex of $T_t$ in a local numbering system, and $\chi_t(x,y)$ is the characteristic function of $T_t$, i.e. $\chi_t(x,y)=1$ if $(x,y)\in T_t$, $\chi_t(x,y)=0$ elsewhere. This approach is the natural method for evaluating velocities in FE-P1 schemes. It is also the most accurate, if no additional post processing is exploited.

*Remark*
The tangential components of the FE-P1 gradient $\nabla p^{(\mathrm{FE})}=-K_t^{-1}\mathbf{v}_t^{(\mathrm{FE})}$ are continuous across inter-element boundaries of each triangle, $T_t$, as opposed to the normal components of both the gradient, $\nabla p^{(\mathrm{FE})}$, and the velocity, $\mathbf{v}_t^{(\mathrm{FE})}$. This implies that $\mathbf{v}^{(\mathrm{FE})}$ satisfies the mass balance equation (1) only in the weak sense [22]. Then, we expect that mass balance errors go to zero in the limit with the same convergence rate as the numerical error. We will see that this is true if we calculate the norm of the errors elementwise, while if we consider alternative subdomains (or element patches) we obtain local mass balances (LMBs) that are exact up to the residual of the linear system solution. This is the property that characterizes a locally conservative scheme [24].

### 2.2. Mixed MHFE discretization

Our MFE formulation uses the classical RT0 basis functions [11] together with hybridization for the solution of the resulting linear system of discrete equations [13]. This implementation follows the details described in [23]. The unknowns of the differential system are the pressure $p$, the Lagrange multipliers $\lambda$, and the velocity field $\mathbf{v}$. They are approximated by

$$p(x,y)\approx p^{(\mathrm{MH})}=\sum_{t=1}^{M} p_t\phi_t$$

$$\lambda(x,y)\approx \lambda^{(\mathrm{MH})}=\sum_{e=1}^{E} \lambda_e\mu_e$$

$$\mathbf{v}(x,y)|_{T_t}\approx \mathbf{v}^{(\mathrm{MH})}|_{T_t}=\sum_{e=1}^{3} q_e\mathbf{w}_{e,t}$$

where $\phi_t$ and $\mathbf{w}_{e,t}$ are the RT0 basis functions, being $\phi_t$ defined elementwise, whereas $\mu_e$ and $\mathbf{w}_{e,t}$ are edgewise. We denote by $\mathbf{p}=\{p_t\}$ the vector of elemental pressures, whereas $\mathbf{q}=\{q_e\}$ is the vector of edge fluxes, and $\boldsymbol{\lambda}=\{\lambda_e\}$ is the vector of Lagrange multipliers. The RT0-P0 discretization leads to the following linear system of algebraic equations:

$$\begin{pmatrix} A & -B & C \\ B^{\mathrm{T}} & 0 & 0 \\ C^{\mathrm{T}} & 0 & 0 \end{pmatrix}\begin{pmatrix} \mathbf{q} \\ \mathbf{p} \\ \boldsymbol{\lambda} \end{pmatrix}=\begin{pmatrix} \mathbf{d} \\ \mathbf{f} \\ \mathbf{g} \end{pmatrix} \tag{4}$$

the matrix is built by the following blocks: $A=\mathrm{diag}[A_1,\ldots,A_M]$, $B=\mathrm{diag}[B_1,\ldots,B_M]$, $C=[C_1^{\mathrm{T}}|C_2^{\mathrm{T}}|\ldots|C_M^{\mathrm{T}}]^{\mathrm{T}}$. Assume $i,k=1,2,3$ are local edge numbering indices; $e=1,\ldots,E$ is the global edge index; $t=1,\ldots,M$ is the global triangle index; moreover, set $r=3(t-1)+i$. The elements of the block matrices can be written as:

$$A_t=(a_{ik}^{(t)}),\quad B_t=(b_i^{(t)}),\quad C_t=(c_{ke}^{(t)}),\quad \mathbf{p}=(p_t),\quad \mathbf{q}=(q_e)$$

$$\mathbf{d}=(d_i^{(t)}),\quad \mathbf{f}=(f_t)$$

$$a_{ik}^{(t)}=\int_{T_t} K_t^{-1}\mathbf{w}_{i,t}\cdot\mathbf{w}_{k,t}\,\mathrm{d}x\,\mathrm{d}y,\quad b_i^{(t)}=\int_{T_t}\mathrm{div}\,\mathbf{w}_{i,t}\,\mathrm{d}x\,\mathrm{d}y$$

$$c_{ke}^{(t)}=\delta_{kr},\quad f_t=\int_{T_t} f(x,y)\,\mathrm{d}x\,\mathrm{d}y$$

$$d_i^{(t)}=-\sum_{t=1}^{M}\int_{E_i}\bar{p}_i\mathbf{w}_{i,t}\cdot\mathbf{n}_{i,t}\,\mathrm{d}s$$

In the previous expressions, the vector $\mathbf{n}_{i,t}$ denotes the outward unit normal to edge $E_i$ of triangle $T_t$, while $\mathbf{g}$ accounts for Neumann boundary conditions. The edge pressure $\bar{p}_i$ is assumed to be zero inside the domain and on the Neumann portion of $\partial\Omega$; hence, $d_i^{(t)}$ is non-zero only if $E_i$ is a Dirichlet boundary edge. The size of the final linear system equals the number of mesh edges.

The linear system (4) can be block solved for the unknown $\boldsymbol{\lambda}$ resulting in:

$$C^{\mathrm{T}}ZC\boldsymbol{\lambda}=C^{\mathrm{T}}SH^{-1}\mathbf{f}-C^{\mathrm{T}}Z\mathbf{b}^{(\mathrm{D})}$$

where $H = B^{\mathrm{T}} A^{-1} B$, $S = A^{-1} B$, and $Z = A^{-1} - S H^{-1} S^{\mathrm{T}}$. Performing these computations involves calculating the inverse of a block diagonal matrix with $3 \times 3$ blocks, which is a trivial matter. The ensuing system matrix is sparse symmetric and positive definite. It can be efficiently solved using the conjugate gradient method [13, 22], preconditioned by the incomplete Cholesky factor [27]. Once $\boldsymbol{\lambda}$ is computed, $\mathbf{p}$ and $\mathbf{v}$ are easily obtained (see, for example [13, 23, 28] for details).

*Remark*

Each Lagrange multiplier $\lambda_e$, which is constant on mesh edge $E_e$, supplies an approximation of the pressure trace at $E_e$ [13]. If there are no sources or sinks, one can show that when the value of the Lagrange multiplier on each edge $E_e$ of $T_t$ is assigned to the midpoint of $E_e$, the resulting three points defined in $\mathbb{R}^3$ span the plane parallel to the pressure gradient [5, 17, 28]. As a result, the RT0-P0 velocity field $\mathbf{v}^{(\mathrm{MH})}$ is constant over each triangle. RT0-P0 velocities have the same convergence rate of FE-P1 and are closely related, as shown, e.g. in [29]. Note that in general the normal component of the RT0-P0 velocity is continuous across inter-element boundaries, whereas the tangential component of the gradient is discontinuous. As opposed to the FE-P1 approach, the discrete velocity field is inherently locally mass conserving, since $\mathbf{v}^{(\mathrm{MH})}$ satisfies the LMB relationship:

$$\int_{\partial T_t} \mathbf{v}_t^{(\mathrm{MH})} \cdot \mathbf{n} + \int_{T_t} f = 0$$

## 3. ERRORS IN THE NUMERICAL VELOCITY FIELDS

Theoretically, the discrete gradients arising from both FE-P1 and RT0-P0 numerical discretizations show first-order accuracy, i.e. the errors in the appropriate Hilbert norms converge proportionally to the mesh characteristic length $h$. However, at fixed mesh sizes, the errors actually displayed by the two schemes can be drastically different. *A posteriori* error estimates give some information on the quality of the discrete flow field, but they are influenced by the smoothness of the true solution. At $K$ interfaces, where the true solution may display large discontinuities in its gradients, these estimates are just rough approximations, since the error constant can be very large. As such, we would like to use some more fundamental properties of the original continuous problem as error indicators. Two important characteristics of the exact field $\mathbf{v}$ that can be used for this purpose are flux balances within closed subsets of $\Omega$, and the behavior of trajectories of ideal particles.

### 3.1. LMB errors

Let $\mathscr{C}$ be the set of all closed, simply connected regions $C \subset \Omega$, with a sufficiently smooth boundary $\partial C$, so that the outward unit normal $\mathbf{n}$ is well defined on $\partial C$, except at most for a finite number of points. Note that when $K$ is discontinuous, yet constant on each triangle, Gauss and Green theorems hold true for the exact velocity $\mathbf{v}$ [30]. Gauss divergence theorem ensures that

$$\mathbb{F}_C = \int_{\partial C} \mathbf{v} \cdot \mathbf{n} \, \mathrm{d}s = \int_C \nabla \cdot \mathbf{v} \, \mathrm{d}x \, \mathrm{d}y = \int_C f(x, y) \, \mathrm{d}x \, \mathrm{d}y \tag{5}$$

An admissible discrete velocity field should satisfy relation (5). The amount by which this equation is not satisfied is called the LMB error. FE-P1 and RT0-P0 discrete velocity fields do not satisfy

DOI: 10.1002/fld

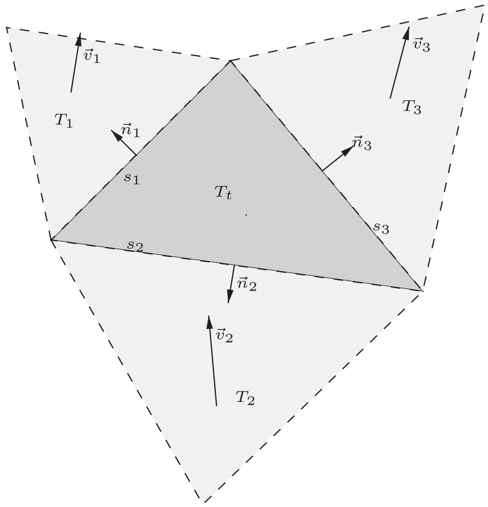

Figure 1. A triangle, $T_t$, and its adjacent elements, $T_k$, $k=1,2,3$. The vector $\mathbf{v}_k$ corresponds to the value of a sample velocity field $\mathbf{v}$ on the triangle $T_k$. The outward normal, $\mathbf{n}_k$, to each side $s_k$ is also shown.

relation (5) on every region $C \in \mathscr{C}$; or in other words, there exist regions $C \in \mathscr{C}$ where the discrete velocity field is affected by the LMB errors. We now consider a few of such regions for which a reasonable LMB error estimator can be defined.

Let $C = T_t$, i.e. let us consider one mesh triangle. An estimate of the flux balance, $\tilde{\mathbb{F}}_{T_t}$, can be computed using the velocities on the adjacent triangles. As an example, the flux balance through the triangle $T_t$ in Figure 1 can be computed as:

$$\tilde{\mathbb{F}}_{T_t} = \sum_{S \in \partial T_t} |S| \mathbf{v}_s \cdot \mathbf{n} \tag{6}$$

where for each side $S \in \partial T_t$, $\mathbf{v}_s$ is the velocity inside $T_s$, which is the triangle sharing side $S$ with $T_t$. Perfect LMB dictates that the quantity $\tilde{\mathbb{F}}_{T_t}$ should be always zero, except for the boundary edges where a Dirichlet condition or a non-zero Neumann flux is imposed. In this case, $\tilde{\mathbb{F}}_{T_t}$ gives the total flux entering or exiting the domain through this edge. Incidentally, note that if in formula (6) we use $\mathbf{v}_t$ in place of $\mathbf{v}_s$, we always obtain $\tilde{\mathbb{F}}_{T_t} = 0$, since $\mathbf{v}_t$ is constant. Since $\mathbf{v}_s^{(\mathrm{MH})} \cdot \mathbf{n} = \mathbf{v}_t^{(\mathrm{MH})} \cdot \mathbf{n}$ by construction, RT0-P0 always displays perfect LMB.

Let us now consider the circulation:

$$\mathbb{C}_C = \int_{\partial C} \mathbf{v} \cdot \mathbf{t} \, \mathrm{d}s \tag{7}$$

where $\mathbf{t}$ is the counterclockwise tangent field to $\partial C$. The circulation must be zero due to Green's second theorem:

$$\int_{\partial C} \mathbf{v} \cdot \mathbf{t} \, \mathrm{d}s = \int_C (\nabla \times \mathbf{v}) \cdot \mathbf{n} \, \mathrm{d}S = \int_C \left( \frac{\partial v_y}{\partial x} - \frac{\partial v_x}{\partial y} \right) \mathrm{d}x \, \mathrm{d}y = 0$$

where **n** is the unit vector normal to the $x$–$y$ plane. Note that this result applies because $\partial C$ is a closed curve and the curl of **v** is zero, since we deal with potential flow. When a piecewise constant vector field **v** is given, the circulation through the triangle $T_t$ in Figure 1 can be approximated by:

$$\tilde{\mathbb{C}}_{T_t} = \sum_{S \in \partial T_t} |S| \mathbf{v}_s \cdot \mathbf{t} \tag{8}$$

where again $\mathbf{v}_s$ is the velocity inside $T_s$, which is the triangle sharing side $S$ with $T_t$. Clearly, **t** is the tangential field to $\partial T_t$.

We now consider a different polygonal mesh region $C$ for the flux balance calculation. Assume that the mesh $\mathscr{T}$ is a Delaunay triangulation [31], where no circumcenters of boundary elements fall outside $\Omega$. Let us consider the Voronoi tessellation set, $\mathscr{V} = \bigcup_{j=1}^{N} V_j$, associated with our mesh nodes. Each Voronoi cell $V_j$ is associated with the mesh node $P_j$ and consists of the points $Q$, such that $d(Q, P_j) \leqslant d(Q, P_k)$ for $k = 1, \ldots, N$, $k \neq j$. Note that the Voronoi cells associated with the internal nodes are bounded, whereas the ones pertaining to the boundary nodes are unbounded. To overcome the unboundedness problem, we take the intersections of the boundary cells with the domain $\Omega$, so that the new set, $\mathscr{V}_{\mathrm{B}}$, is made up of all bounded cells. The boundary, $\partial V_j$, of each $V_j \in \mathscr{V}_{\mathrm{B}}$ is the union of the segments connecting the circumcenters of two adjacent triangles sharing node $N_j$. All the other entities are defined in Figure 2.

The set $\tau^{(j)}$ of all triangles sharing the node $N_j$ forms a nodal cell, called a $T$-cell. We can also construct a yet different nodal cell as follows. For any given $T_t \in \tau^{(j)}$, let $t_i^{(j)}$ be the triangle identified by node $N_j$ and the midpoints of the edges belonging to $T_t$, which share $N_j$. The union

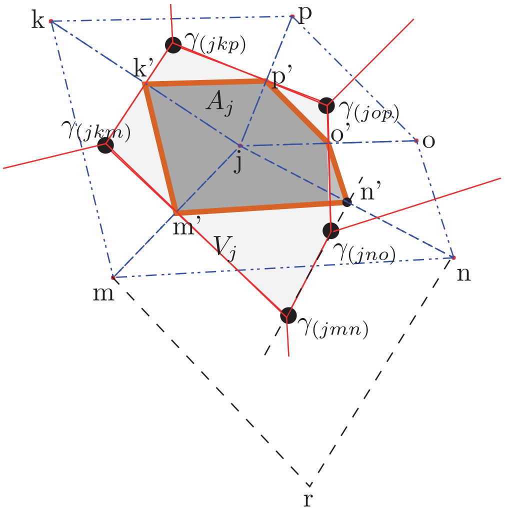

Figure 2. Portion of a sample Delaunay mesh. The triangles sharing node $j$ are shown by dashed-dotted lines. A further mesh triangle, $(mnr)$, is identified by dashed lines. The Voronoi cell, $V_j$, centered on node $j$ is filled by light shade. The $A$-cell $A_j$ associated with node $j$ is pointed out by darker shade. The circumcenter of each triangle is identified by the Greek letter $\gamma$; the edge midpoints are denoted by an apostrophe.

DOI: 10.1002/fld

of such triangles forms the alternative cell ($A$-cell, for short), $A_j$ (see Figure 2). We denote by $\mathscr{A}_{\mathrm{I}}$ the set consisting of the $A$-cells associated with internal mesh nodes.

Let us denote by $\sigma_{jk}^{(jkm)}$ the elemental linear Galerkin stiffness coefficient defined on triangle $T_t=(jkm)$, and pertaining to edge $jk$. One has

$$\sigma_{jk}^{(jkm)}=\int_{(jkm)} K_{(jkm)}\nabla\xi_j\cdot\nabla\xi_k\,\mathrm{d}x\,\mathrm{d}y$$

Referring to the triangles in Figure 2, one can prove that [7, 16]

$$\sigma_{jk}^{(jkm)}=-K_{(jkm)}\frac{|k'\gamma_{(jkm)}|}{|jk|},\qquad \sigma_{jk}^{(jkp)}=-K_{(jkp)}\frac{|k'\gamma_{(jkp)}|}{|jk|} \tag{9}$$

The left-hand side of the first equation in (9) represents the flux through the line segment $k'\gamma_{(jkm)}$, which connects points $k'$ and $\gamma_{(jkm)}$ due to a unitary pressure difference between the nodes $N_k$ and $N_j$ [16]. On the ground of these relationships, one can prove that [7, 32]

$$\sigma_{jk}^{(jkm)}=\int_{(jkm)} K_{(jkm)}\nabla\xi_j\cdot\nabla\xi_k\,\mathrm{d}x\,\mathrm{d}y=\int_{\eta}-K_{(jkm)}\nabla\xi_j\cdot\mathrm{d}\mathbf{n} \tag{10}$$

where $\eta=m'\gamma_{(jkm)}\cup k'\gamma_{(jkm)}$, and $\mathbf{n}$ is the normal to $\eta$, pointing opposite to $j$. Since the integral in (10) depends only on the endpoints $m'$ and $k'$, we can choose a different segment $\eta'=m'k'$ to obtain

$$\int_{\eta'}-K_{(jkm)}\nabla\xi_j\cdot\mathrm{d}\mathbf{n}=\int_{\eta}-K_{(jkm)}\nabla\xi_j\cdot\mathrm{d}\mathbf{n}=\sigma_{jk}^{(jkm)} \tag{11}$$

Working on triangle $(jkm)$ and using relation (3), we obtain

$$\sigma_{jm}^{(jkm)}p_m+\sigma_{jk}^{(jkm)}p_k+\sigma_{jj}^{(jkm)}p_j=\int_{\eta'}\mathbf{v}_{(jkm)}^{(\mathrm{FE})}\cdot\mathrm{d}\mathbf{n}$$

Repeating this procedure for all triangles sharing node $j$ we find that the $j$th FE-P1 equation represents the flux through the boundary, $\partial A_j$, of the $A$-cell $A_j$. Hence, the $j$th equation can be written as:

$$\begin{aligned}\sum_{T\in\tau^{(j)}}\sum_{N_i\in V(T)}\sigma_{ji}^{(t)}p_i&=\sum_{S\in\partial A_j}\int_S\mathbf{v}_t^{(\mathrm{FE})}\cdot\mathrm{d}\mathbf{n}\\&=\sum_{T_t\in\tau^{(j)}}\int_{T_t}f(x,y)\xi_j(x,y)\,\mathrm{d}x\,\mathrm{d}y\end{aligned} \tag{12}$$

where $V(T)$ is the set of the vertices of triangle $T$, $\mathbf{v}_t^{(\mathrm{FE})}$ is the velocity on triangle $T_t\in\tau^{(j)}$, and $\mathbf{n}$ is the outward normal to $A_j$. Thus, FE-P1 can be viewed as a sub-domain collocation approach or equivalently except for the right-hand side and the discretization of the diffusion coefficient, as a FV method defined on Voronoi cells. Since the basis functions are harmonic, we can view FE-P1 as equivalent to FV defined on $A$-cells as well, and use the latter cells as they are easier to calculate. Similar results but on different subdomains were proved also in [14, 15, 32]. The LMB characteristics of the FE-P1 and RT0-P0 approach can be evaluated by looking at the discrete fluxes calculated by integrating $\mathbf{v}^{(\cdot)}\cdot\mathbf{n}$ along the boundary $\partial A_j$. For a piecewise constant vector field $\mathbf{v}$, the flux and circulation through $A_j$ are given by

$$\tilde{\mathbb{F}}_{A_j}=\sum_{S\in\partial A_j}|S|\mathbf{v}_t\cdot\mathbf{n},\quad \tilde{\mathbb{C}}_{A_j}=\sum_{S\in\partial A_j}|S|\mathbf{v}_t\cdot\mathbf{t} \tag{13}$$

where each $S$ is the line segment in $\partial A_j$ that lies inside triangle $T_t\in\tau^{(j)}$. Each boundary piece $S\in T_t$ is half as long as the corresponding parallel piece of $\partial\tau^{(j)}$, so that the discrete flux on $A_j$ is half the flux on the $T$-cell $\tau^{(j)}$, i.e.

$$\tilde{\mathbb{F}}_{A_j}=\frac{1}{2}\sum_{S\in\partial\tau^{(j)}}|S|\mathbf{v}_t\cdot\mathbf{n}=\frac{1}{2}\tilde{\mathbb{F}}_{\tau^{(j)}}$$

$$\tilde{\mathbb{C}}_{A_j}=\frac{1}{2}\sum_{S\in\partial\tau^{(j)}}|S|\mathbf{v}_t\cdot\mathbf{t}=\frac{1}{2}\tilde{\mathbb{C}}_{\tau^{(j)}}$$

Extending these results to Voronoi cells would imply the definition of a modified velocity field to take into consideration the case when a circumcenter lies outside the triangle (for example, see the circumcenter $\gamma_{(jmn)}$ in Figure 2).

Note that Delaunay meshes on two-dimensional linear Galerkin FE-P1 guarantee that a discrete maximum principle holds, which implies monotone convergence and local conservation properties for the numerical scheme [7, 16]. Unfortunately, this result does not carry over to three-dimensional FE-P1. Numerical experiments suggest that also for RT0-P0 the Delaunay property is sufficient for monotonicity in 2D triangulations [33].

### 3.2. Particle tracking

The comparison between the behavior of $\mathbf{v}^{(\mathrm{FE})}$ and $\mathbf{v}^{(\mathrm{MH})}$ can be carried out by analyzing the streamlines calculated as trajectories of ideal particles driven by the two velocity fields. We compute a set of approximate trajectories and perform statistical considerations to analyze the accuracy of the discrete velocity fields, i.e. their 'mean' difference from the exact field $\mathbf{v}$. To this aim, assume that the exact (stationary) velocity field $\mathbf{v}(x,y)=(v_x(x,y),v_y(x,y))$ of Equation (2) is available. The trajectory $X(t)=(x(t),y(t))$, $x,y\in\Omega$ of a unit mass particle is obtained by

$$x(t)=x(t_0)+\int_{t_0}^{t}v_x\,\mathrm{d}t,\quad y(t)=y(t_0)+\int_{t_0}^{t}v_y\,\mathrm{d}t \tag{14}$$

Piecewise linear approximation $\tilde{X}$ of a particle trajectory $X$ is obtained by releasing the particle at the starting point $(x_0,y_0)$, assumed to belong to triangle $T$, and computing the point where the line parallel to $\mathbf{v}$, through the starting point, intersects the boundary of $T$. The set of the approximated trajectory points, $\tilde{X}=(\tilde{x}_i,\tilde{y}_i)$, is given by

$$\tilde{x}_i=x_0+\sum_{j=0}^{i}v_x\Delta t_j,\quad \tilde{y}_i=y_0+\sum_{j=0}^{i}v_y\Delta t_j \tag{15}$$

where $\Delta t_j=t_{j+1}-t_j$, $t_j$ is the time when the particle hits the boundary of the $j$th triangle visited by the path, and the first triangle ($j=0$) contains the starting point. The trajectory is stopped when it reaches the domain boundary. This last condition is not guaranteed to be fulfilled. Some exceptional cases must be managed. Suppose that the particle $P$ is on the boundary of a mesh triangle $T_t$. $P$ is moved along the direction of the velocity $\mathbf{v}_t$ until it reaches a point $Q$ on the opposite boundary piece of $T_t$. One of the following cases can occur:

1. $Q$ can be a mesh node. In this case, more than one mesh triangle shares $Q$, and the velocity field is not unique. The path is then stopped and considered as aborted path. Aborted paths do not enter our statistical considerations. In principle, we could devise some sort of field averaging, identify a feasible velocity vector, and let the path go on. We did not use this approach, in order to avoid possible biases introduced in the statistics by this averaging procedure.
2. $Q$ is a boundary point. The trajectory is stopped and added as a valid path to our set.
3. $Q$ is neither a boundary point, nor a mesh node. In this case, the path is driven inside the adjacent triangle $T_r$ sharing point $Q$ with $T_t$. Two different situations can occur:
    (a) $\mathbf{v}_r$ (the velocity inside $T_r$) points outward from $T_r$, and it will move particle $P$ back into triangle $T_t$; the path is stopped and labeled as aborted path, as by continuing this procedure we will end up calculating a trajectory that eventually will hit a node of $T_t$ and case 1 applies.
    (b) in all other cases the path-line calculation proceeds and $P$ is driven by $\mathbf{v}_r$ inside $T_r$.

Our tracking procedure continues until a path either aborts or reaches the boundary.

## 4. NUMERICAL RESULTS

Our test problems are based on solving problem (1) on the unit square $\Omega=[0,1]^2$, with $f(x,y)=0$. Dirichlet boundary condition $p=1$ is set on the $x=0$ side of the domain. The outflow boundary is represented by a Dirichlet condition $p=0$ on the window $x=1$, $0.3\leqslant y\leqslant 0.7$ (see Figure 3, left frame). The remaining part of the boundary is impervious, i.e. Neumann boundary conditions $\partial p/\partial\mathbf{n}=0$ are set.

In the solution of the linear systems, convergence of the Choleski-Preconditioned Conjugate Gradient iteration is considered achieved when the relative residual of the final solution falls below a tolerance, set equal to $10^{-15}$. Note that the mass balance errors, if evaluated using the correct control volumes, are theoretically of the same order of magnitude of this tolerance. We acknowledge that the use of such a small tolerance is generally not warranted and much lower tolerances can be safely used leading to savings in computational time. However, we force such a small value for the final residual in order to avoid problems that may arise (e.g. in the heterogeneous test cases) with badly scaled matrices.

We start our analysis with a homogeneous problem, i.e. a constant diffusion coefficient $K$. Next, we consider a heterogeneous problem featuring two pillars (i.e. the rectangles $[0.3,0.4]\times[0.0,0.7]$ and $[0.6,0.7]\times[0.3,1.0]$) bearing a much lower diffusion coefficient, $K'=10^{-6}K$ (see Figure 3, on left).

We initially discretize the domain by a Delaunay triangulation, $\mathscr{T}^{(0)}$, consisting of 217 elements, 127 nodes, 343 edges, obtained by means of Matlab routines [34]. Figure 3, left, shows the mesh and the corresponding boundary conditions. Figure 4 shows the dual Voronoi tessellation (left) and the $A$-cells (right). The subsequent $\mathscr{T}^{(\ell)}$, $\ell=1,2,3$, meshes are obtained by uniform refinement of $\mathscr{T}^{(0)}$, yielding 868, 3472, 13 888 elements; 470, 1807, 7085 nodes; 1337, 4184, 20 972 edges,

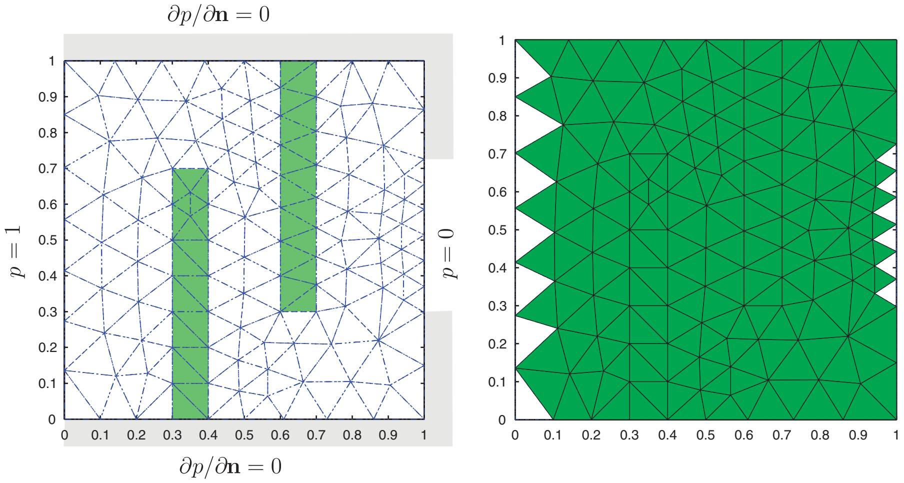

Figure 3. Delaunay mesh $\mathscr{T}^{(0)}$ (left frame) and corresponding boundary conditions. Two rectangles, which in our heterogeneous case are lower diffusion zones, have been darkened. In the right frame, the triangles in $\mathscr{T}_F^{(0)}$ are darkened.

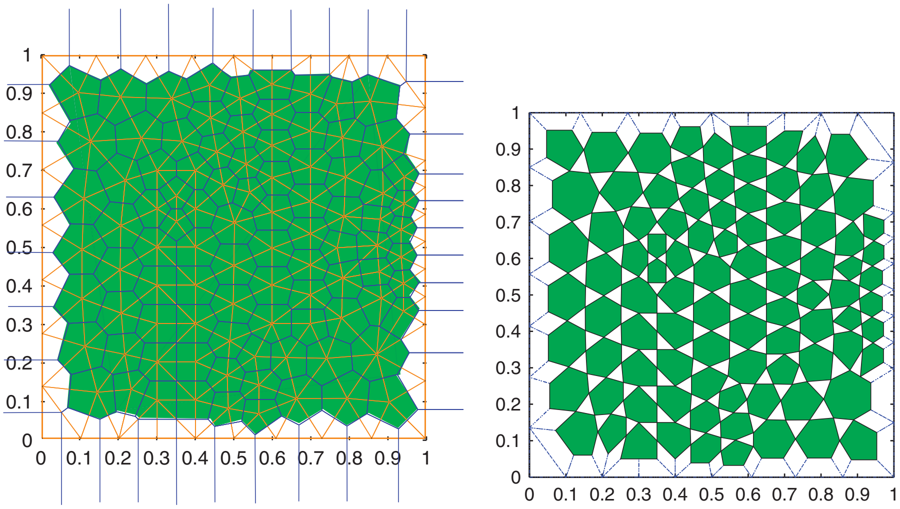

Figure 4. Left frame: dual Voronoi cells (solid lines) for the Delaunay mesh $\mathscr{T}^{(0)}$. The bounded Voronoi cells have been darkened. Right frame: the internal $A$-cells, $A_j^{(0)}$.

respectively. The meshes are characterized by a balance ratio [35] of about 0.34, which is not far from the optimal value of $1/\sqrt{3}$ attained by equilateral triangles.

Recall that the FE-P1 final linear system size is equal to the number of mesh nodes, whereas the RT0-P0 system size is equal to the number of mesh edges. One could argue that a sound comparison between FE-P1 and RT0-P0 characteristics should be carried over by exploiting one mesh for

FE-P1, another for RT0-P0, chosen so that the size of the two systems are approximately equal. In order to address this issue, we also considered two more Delaunay triangulations obtained by Matlab routines, $\check{\mathscr{T}}^{(0)}$ and its uniform refinement, $\check{\mathscr{T}}^{(1)}$. The mesh $\check{\mathscr{T}}^{(0)}$ has 378 nodes, i.e. almost as many edges as $\mathscr{T}^{(0)}$, and 1063 edges. On the other hand, $\check{\mathscr{T}}^{(1)}$ consists of 2744 elements, 1441 nodes, and 4184 edges to be compared with $\mathscr{T}^{(1)}$ that is characterized by 868 elements and 1337 edges.

### 4.1. *Behavior of the LMB errors*

First, let us focus on the $\mathscr{T}^{(\ell)}$, $\ell=0,1,2,3$ meshes. Let us define the set $\mathscr{T}_{\mathrm{F}}^{(\ell)}$ of $F$-triangles, where 'F' stands for 'zero Flow'. The set consists of those triangles, which either are 'internal' (i.e. they belong to the subset $\mathscr{T}_{\mathrm{I}}^{(\ell)}$ of those triangles that do not have boundary edges), or have impervious boundary edges. Figure 3, left, shows the $F$-triangles in $\mathscr{T}^{(0)}$.

Recall that in our homogeneous test problem, the exact fluxes and circulations satisfy

$$\mathbb{F}_T=0, \quad \mathbb{C}_T=0 \ \forall T\in\mathscr{T}, \quad \mathbb{F}_A=0, \quad \mathbb{C}_A=0 \ \forall A\in\mathscr{A}_{\mathrm{I}}$$

Figure 5 shows the absolute values of the numerical fluxes, $|\tilde{\mathbb{F}}_T^{(\cdot,0)}|$, calculated by the FE-P1 and RT0-P0 discrete velocity fields obtained on the $F$-triangles, $T\in\mathscr{T}_{\mathrm{F}}^{(0)}$. The fluxes are computed using Equation (6). Each value, $|\tilde{\mathbb{F}}_T|$, is associated to the centroid of $T$, $(x_c, y_c)$, and the projection of the point $(x_c, y_c, |\tilde{\mathbb{F}}_T|)$ onto the $y=0$ plane is plotted. The results show that the $|\tilde{\mathbb{F}}_T^{(\mathrm{FE},0)}|$ fluxes are not negligible, according to the discussion reported in Section 3.1. On the other hand, the fluxes through the same $F$-triangles, $\tilde{\mathbb{F}}_T^{(\mathrm{MH},0)}$, as calculated by the RT0-P0 velocity, are numerically zero to double precision accuracy, again in accordance with the discussion in Section 3.1.

Let us now consider the FE-P1 and RT0-P0 fluxes, $|\tilde{\mathbb{F}}_A^{(\cdot,0)}|$, through internal $A$-cells $A\in\mathscr{A}_{\mathrm{I}}^{(0)}$ of mesh $\mathscr{T}^{(0)}$. Figure 6 plots each absolute flux value, $|\tilde{\mathbb{F}}_A^{(\cdot,0)}|$, versus its associated mesh node, i.e. the

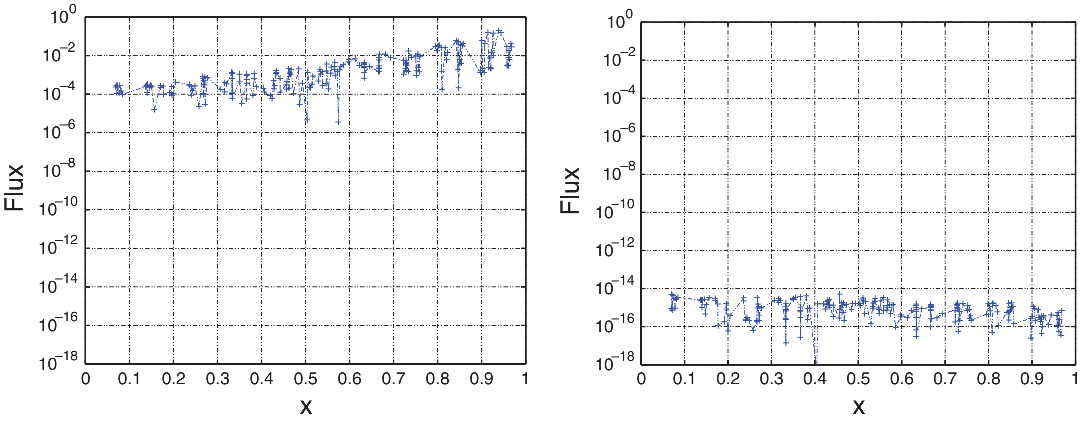

Figure 5. Mesh $\mathscr{T}^{(0)}$, homogeneous problem. Absolute values, $|\tilde{\mathbb{F}}_T|$, of FE-P1 numerical flux (left frame) and RT0-P0 (right frame) through each $F$-triangle $T$. The fluxes are associated to the triangle centroid, $(x_c, y_c)$, and the projection onto the $x$–$z$ plane of each point $(x_c, y_c, |\tilde{\mathbb{F}}_T|)$ is plotted.

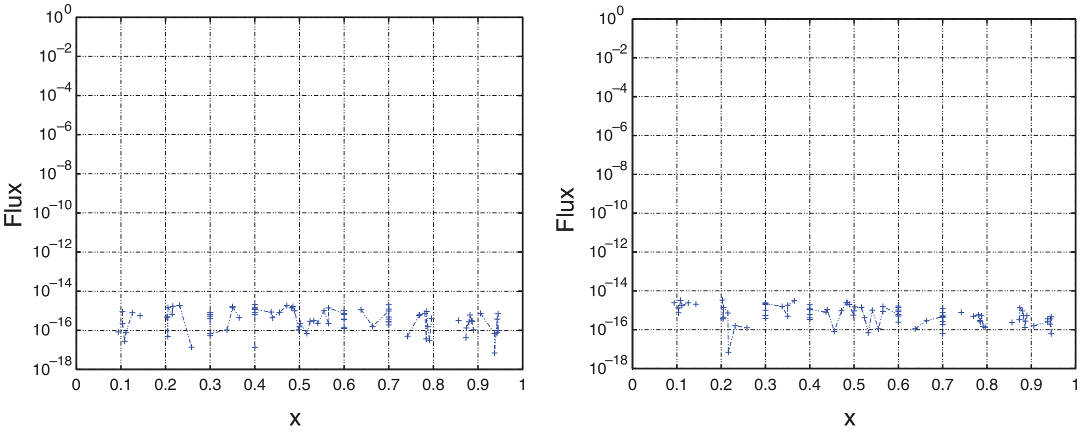

Figure 6. Mesh $\mathscr{T}^{(0)}$, homogeneous problem, FE-P1 (left frame) and RT0-P0 (right frame) absolute fluxes through internal $A$-cells. The absolute flux through cell $A_j$ is plotted onto the $x$–$z$ plane versus the abscissa of node $j$.

projection of the point $(x, y, |\tilde{\mathbb{F}}_A^{(\cdot,0)}|)$ onto the $y=0$ line. It can be noted that the FE-P1 and RT0-P0 fluxes are negligible, up to double precision, on all cells in $\mathscr{A}^{(0)}$. This result shows that FE-P1 can be considered as a locally conservative method, i.e. mass conservation is guaranteed when calculated on the correct local control volume, contrary to statements found also in the recent literature [24].

Let us now consider the heterogeneous problem. The circulation calculated from FE-P1 on triangles is not negligible, as opposed to the homogeneous case. The same applies to both FE-P1 and RT0-P0 circulations on $A$-cells. Figure 7 (left) shows the triangles where FE-P1 circulation is non-negligible. Figure 7 (right) shows the nodes associated to non-negligible RT0-P0 circulation on internal $A$-cells. The Figures show that non-negligible FE-P1 circulation on triangles are observed around the boundary of the pillars, where changes in the diffusion coefficient are displayed. Non-zero circulations are raised also on triangles touching the no-flow Neumann boundary edges, where the flow is strictly tangential. Similar results arise from RT0-P0 circuitation on $A$-cells.

Given a mesh level, $\ell$, let $\phi$ indicate a measure of the LMB error (either $\phi=\mathbb{F}$ or $\phi=\mathbb{C}$) that occurs either on internal triangles $T\in\mathscr{T}_{\mathrm{I}}^{(\ell)}$ (denoted by $\phi_{T,\ell}$), or on internal $A$-cells $A\in\mathscr{A}_{\mathrm{I}}^{(\ell)}$ (denoted by $\phi_{A,\ell}$). The $L_2(\mathscr{T}^{(\ell)})$ error norm is calculated either on triangles or on $A$-cells can be approximated by the discrete balances

$$L_{T,\phi}^{(\ell)}=\left(\sum_{T\in\mathscr{T}_{\mathrm{I}}^{(\ell)}}|\phi_{T,\ell}|^2|T|\right)^{1/2}, \quad L_{A_i,\phi}^{(\ell)}=\left(\sum_{A_i\in\mathscr{A}_{\mathrm{I}}^{(\ell)}}|\phi_{A_i,\ell}|^2\frac{|\tau^{(i)}|}{3}\right)^{1/2} \tag{16}$$

where $|\tau^{(i)}|/3$ is the area pertaining to node $i$. The values of $\phi_{\cdot,\ell}$ are calculated on the corresponding geometrical regions, using either the normal fluxes ($\phi=\tilde{\mathbb{F}}$) or the tangential fluxes ($\phi=\tilde{\mathbb{C}}$), yielding the $L_{\cdot,\mathbb{F}}$ and $L_{\cdot,\mathbb{C}}$ norms, respectively.

The numerical results are summarized in Table I. Let us consider first the homogeneous case. Again in theory all balances should be zero, since $f(x,y)=0$. Numerical zero is attained when

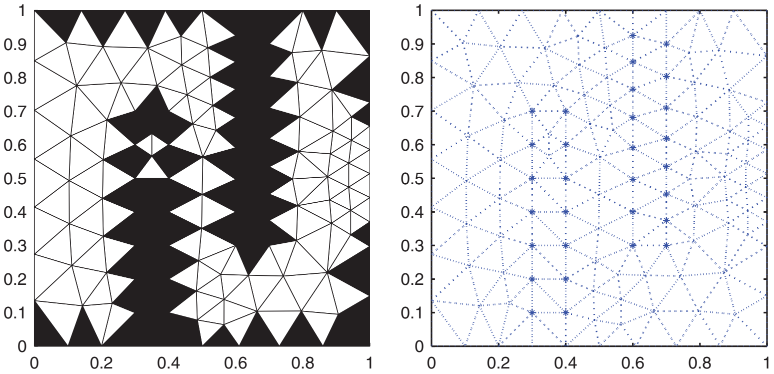

Figure 7. Heterogeneous problem. Right frame: filled triangles indicate a non-negligible $\tilde{\mathbb{C}}_T^{(\mathrm{FE})}$. Left frame: the nodes, where $\tilde{\mathbb{C}}_{A_i}^{(\mathrm{MH})}$ is non-negligible, are shown.

Table I. Approximated values of the $L_2$ norm of balance errors for velocities on internal triangles, $L_{T,\cdot}^{(\cdot,\ell)}$ and on internal $A$-cells, $L_{A,\cdot}^{(\cdot,\ell)}$. $\mathbb{F}$ = (normal) flux, $\mathbb{C}$ = circulation.

| — | | | Homogeneous | | Heterogeneous | |
|---|---|---|---|---|---|---|
| Balance | Alg. | $n_T$ | $L_{T,\cdot}^{(\cdot,\ell)}$ | $L_{A,\cdot}^{(\cdot,\ell)}$ | $L_{T,\cdot}^{(\cdot,\ell)}$ | $L_{A,\cdot}^{(\cdot,\ell)}$ |
| $\mathbb{F}$ | FE-P1 | 217 | 2.69e−02 | 6.92e−16 | 1.49e−02 | 5.78e−16 |
| | | 868 | 9.05e−03 | 7.81e−16 | 4.82e−03 | 1.16e−15 |
| | | 3472 | 3.16e−03 | 1.39e−15 | 1.58e−03 | 1.20e−15 |
| | | 13 888 | 1.12E−03 | 1.60E−15 | 5.27E−04 | 1.47E−15 |
| | RT0-P0 | 217 | 1.49e−15 | 1.14e−15 | 1.59e−15 | 1.05e−15 |
| | | 868 | 1.68e−15 | 1.05e−15 | 1.60e−15 | 1.03e−15 |
| | | 3472 | 2.03e−15 | 1.29e−15 | 1.91e−15 | 1.24e−15 |
| | | 13 888 | 2.55E−15 | 1.54E−15 | 2.36E−15 | 1.43E−15 |
| $\mathbb{C}$ | FE-P1 | 217 | 1.59e−15 | 8.03e−16 | 3.33e−02 | 3.18e−02 |
| | | 868 | 2.91e−15 | 2.28e−15 | 1.18e−02 | 1.18e−02 |
| | | 3472 | 6.14e−15 | 4.12e−15 | 4.29e−03 | 4.22e−03 |
| | | 13 888 | 1.23E−14 | 8.23E−15 | 1.51E−03 | 1.51E−03 |
| | RT0-P0 | 217 | 2.72e−02 | 9.74e−16 | 3.25e−02 | 3.41e−02 |
| | | 868 | 7.97e−03 | 1.19e−15 | 1.18e−02 | 1.24e−02 |
| | | 3472 | 2.63e−03 | 1.35e−15 | 4.32e−03 | 4.42e−03 |
| | | 13 888 | 1.09E−03 | 1.82E−15 | 1.54E−03 | 1.58E−03 |

the discrete balance is of the order $10^{-15}$, which is the tolerance used in our experiments for the solution of our linear systems. On the other hand, when the balances are not satisfied exactly, the corresponding norms decrease at a rate that closely resembles the error convergence rate predicted by theory, as shown in Figure 8. Table I shows that $L_{T,\mathbb{F}}^{(\mathrm{FE},\ell)}$ values are non negligible: FE-P1 does not accomplish flux balance through triangles. This is the reason, why in the literature,

DOI: 10.1002/fld

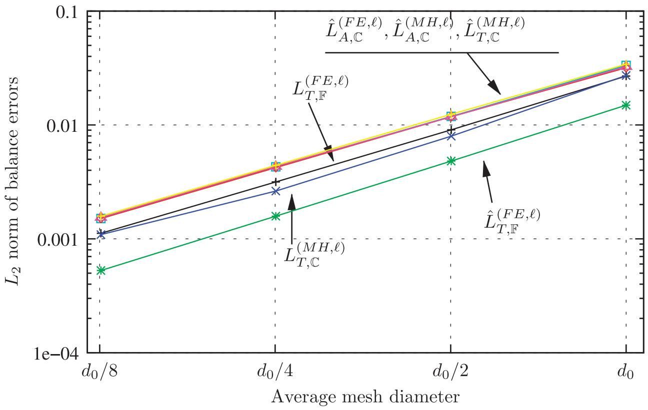

Figure 8. Convergence of the LMB error for FE-P1 and RT0-P0 flux and circulation on internal triangles and $A$-cells. Both the results for the homogeneous problem $L^{(\cdot,\ell)}_{\cdot,\cdot}$ and the heterogeneous case $\hat{L}^{(\cdot,\ell)}_{\cdot,\cdot}$ are considered. FE = Finite Elements, MH = Mixed Hybrid. Numerically zero balances are not plotted.

Table II. Approximated values of the $L_2$ norm of balance errors, when the $\breve{\mathscr{T}}^{(\ell)}$ meshes, $\ell=0,1$, are exploited. Label meanings are the same as in Table I.

| — | | | Homogeneous | | Heterogeneous | |
|---|---|---|---|---|---|---|
| Balance | Alg. | $n_T$ | $L^{(\cdot,\ell)}_{T,\cdot}$ | $L^{(\cdot,\ell)}_{A,\cdot}$ | $L^{(\cdot,\ell)}_{T,\cdot}$ | $L^{(\cdot,\ell)}_{A,\cdot}$ |
| $\mathbb{F}$ | FE-P1 | 686 | 8.44E−03 | 7.68E−16 | 5.81E−03 | 7.40E−16 |
| | | 2744 | 2.97E−03 | 1.09E−15 | 1.80E−03 | 8.73E−16 |
| | RT0-P0 | 686 | 1.69E−15 | 1.13E−15 | 1.60E−15 | 1.02E−15 |
| | | 2744 | 1.92E−15 | 1.19E−15 | 1.79E−15 | 1.11E−15 |
| $\mathbb{C}$ | FE-P1 | 686 | 2.01E−15 | 1.38E−15 | 1.44E−02 | 1.46E−02 |
| | | 2744 | 4.56E−15 | 3.24E−15 | 5.15E−03 | 5.18E−03 |
| | RT0-P0 | 686 | 9.40E−03 | 9.95E−16 | 1.47E−02 | 1.53E−02 |
| | | 2744 | 2.98E−03 | 1.24E−15 | 5.29E−03 | 5.46E−03 |

one finds that FE-P1 is not locally conservative. The opposite is true for $L^{(\mathrm{MH},\ell)}_{T,\mathbb{F}}$, $\ell=0,1,2,3$, which is numerically zero. On the other hand, if we consider the flux through internal $A$-cells, the $L^{(\mathrm{FE},\ell)}_{A,\mathbb{F}}$ values are negligible, as well as $L^{(\mathrm{MH},\ell)}_{A,\mathbb{F}}$, showing that FE-P1 is indeed locally conservative if we look at the correct control volumes, e.g. the $A$-cells.

In the heterogeneous case the results again follow the discussion carried over in Section 3.1. All balances should be zero. It is worth noting that RT0-P0 still achieves exact mass balance while so does FE-P1 only, when the $A$-cells are considered. while RT0-P0 does not.

Table II reports the balance errors for the meshes yielding equal computational costs for the two schemes. It can be easily concluded that the comparison between FE-P1 and RT0-P0 balance fluxes does not change even when more refined meshes are used for FE-P1.

### *4.2. Results of particle tracking experiments*

We started 100 particles at the points $(\bar{x}, \bar{y}_i)$, $\bar{x}=0$, $\bar{y}_i = ih$, $h=1/101$, $i=1,\dots,100$. Note that, due to our boundary conditions, the theoretical trajectories leave the domain on the portion of the right side where $p=0$ (see Figure 3, left). First, let us focus on the $\mathscr{T}^{(\ell)}$, $\ell=0,1,2,3$ meshes. Figures 9 and 10 show the FE-P1 (left) and RT0-P0 (right) trajectories calculated for the homogeneous and heterogeneous test problems, respectively. The paths are driven by the velocity fields $\mathbf{v}^{(\mathrm{FE},0)}$ or $\mathbf{v}^{(\mathrm{MH},0)}$ computed on the mesh $\mathscr{T}^{(0)}$. Note that the paths that ended in the zone marked by 'W' in Figure 9 (left), and 10 (left), suffered wrong exits, as they leave the domain through an impervious portion of the boundary. The results show that the FE-P1 velocity field is not everywhere parallel to the impervious boundaries. Figure 11 draws a detail of the $\mathbf{v}^{(\mathrm{FE},0)}$ field for the homogeneous (left) and the heterogeneous (right) cases. By examining the right portion of the domain, on the

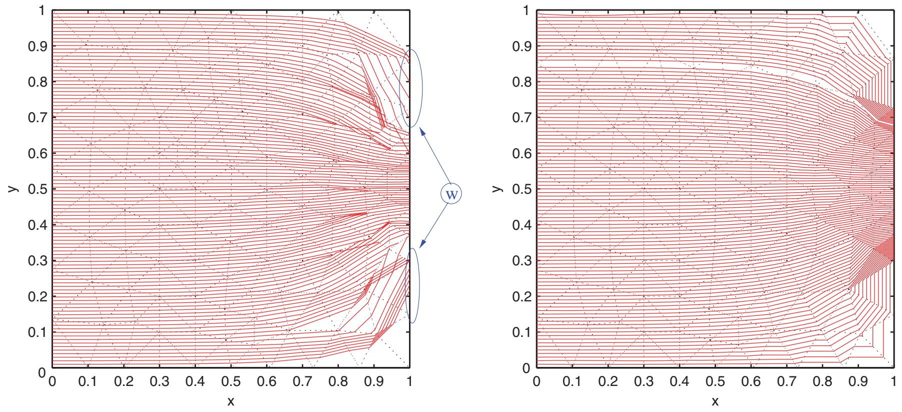

Figure 9. FE-P1 (left) and RT0-P0 (right) path lines evaluated from the numerical velocity fields in the homogeneous case. Regions pointed at by 'W' show zones, where FE-P1 paths exited through an impervious part of the boundary. The mesh is also shown by dotted lines.

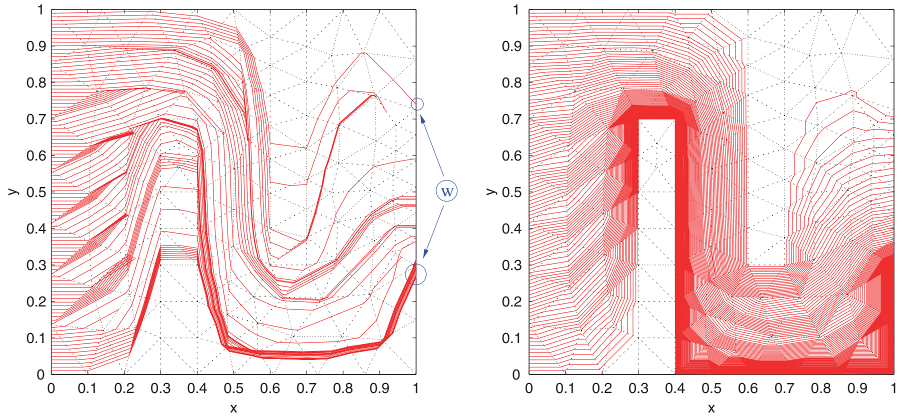

Figure 10. Analogous to the previous figure; path lines obtained in the heterogeneous case are shown.

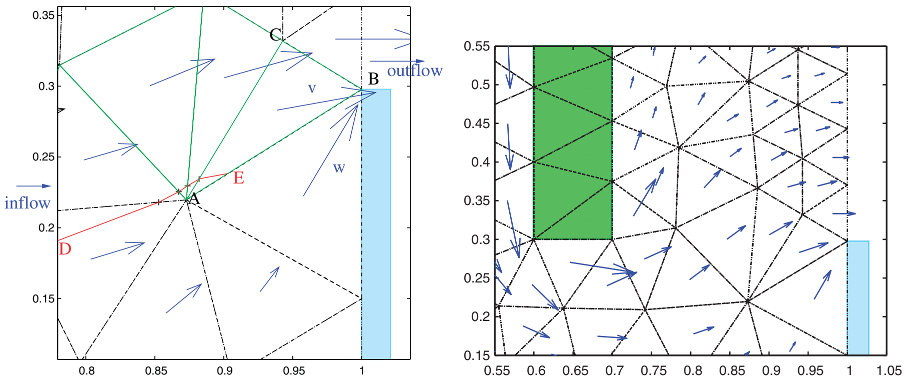

Figure 11. Detail of the FE-P1 path lines and corresponding $\mathbf{v}^{(\mathrm{FE},0)}$ field for the homogeneous (left) and heterogeneous (right) cases shown in Figures 9 and 10.

left frames of Figures 9 and 10, one can see that the FE-P1 field is not parallel to the impervious boundary around the outflow portion. This is the reason for the wrong exit of some FE-P1 trajectories. The RT0-P0 trajectories do not show this phenomenon because of the continuity of the normal component of $\mathbf{v}^{(\mathrm{MH},0)}$ at element edges. Thus, the RT0-P0 velocity field is conservative as opposed to the behavior of FE-P1. However, we would like to stress here that it is the reconstruction of the velocity vector and not the FE-P1 linear Galerkin scheme that is non-conservative. Note that the behavior of velocity fields as shown in Figures 9 and 10 points out the differences between FE-P1 and RT0-P0, showing that the two schemes (or at least one of the two) are affected by errors that are clearly visible.

Looking at the results for the heterogeneous problem in Figure 10, we note that many FE-P1 trajectories enter the slow-diffusion zones, whereas RT0-P0 paths do not. Let us consider the elements that are either adjacent to a slow-diffusion rectangle or fall inside one of them. One expects that the velocity on those elements is almost parallel to the rectangle sides. Instead, while $\mathbf{v}^{(\mathrm{MH},0)}$ is practically parallel to these sides, $\mathbf{v}^{(\mathrm{FE},0)}$ velocity field is not. Inside the rectangles the velocity is very small; hence, parallelism is not crucial, but in the remaining portion of the domain it is an important feature. Non-parallel FE-P1 velocities are located on most of the sides of the two low-conductivity zones. This behavior is a consequence of the fact that FE–P1 mass balance control volumes are defined across $K$ discontinuities.

Another behavior that can be ascribed to the lack of continuity of the components of the FE-P1 flow field normal to triangle edges, is what we denote by decussation of the velocity field. To exemplify this phenomenon, Figure 11 shows an example of a region where the FE-P1 velocity field decussates in both the homogeneous and heterogeneous cases. With reference to the left figure, the normal components of both velocity vectors $\mathbf{v}$ and $\mathbf{w}$ point toward triangle edge AB. Once the trajectory passing through the point D reaches the side AB at point E, the velocity outside triangle ABC takes the particle back inside. Thus, an unfeasible point on the side AB is tracked and we stop the trajectory at point E. Note that decussating does not occur in the RT0-P0 velocity field. RT0-P0 trajectories abort only when they start from or reach a point where the velocity field is non-unique. We should remark that there are several ways to handle these cases of decussation, such as for example continue the trajectory until we reach a node where we can take the average of the velocity vectors that surround this node. However, this approach, exactly like other similar

Table III. Statistics of calculated trajectories. A total of 100 trajectories are evaluated, so that the numbers can be considered as percentages. Legend: $n_T = \#$ of triangles in the mesh; Alg = Algorithm; Cor = # of correct trajectories (non-aborted); Rex = # of Right-exited trajectories; Wex = # of Wrong-exited trajectories; Abr = # of aborted trajectories.

| | | Homogeneous domain | | | | Heterogeneous domain | | | |
|---|---|---|---|---|---|---|---|---|---|
| $n_T$ | Alg | Cor | Rex | Wex | Abr | Cor | Rex | Wex | Abr |
| 217 | FE-P1 | 52 | 42 | 10 | 48 | 42 | 23 | 19 | 58 |
| 868 | FE-P1 | 72 | 65 | 7 | 28 | 49 | 21 | 28 | 51 |
| 3472 | FE-P1 | 75 | 72 | 3 | 25 | 53 | 35 | 18 | 47 |
| 13 888 | FE-P1 | 79 | 76 | 3 | 21 | 66 | 45 | 21 | 34 |
| 217 | RT0-P0 | 100 | 100 | 0 | 0 | 100 | 100 | 0 | 0 |
| 868 | RT0-P0 | 99 | 99 | 0 | 1 | 99 | 99 | 0 | 1 |
| 3472 | RT0-P0 | 100 | 100 | 0 | 0 | 100 | 100 | 0 | 0 |
| 13 888 | RT0-P0 | 96 | 96 | 0 | 4 | 96 | 96 | 0 | 4 |

ones, introduces biases in the trajectory with respect to the PDE solution, and on purpose is not considered in the present paper, even though it is suggested for practical applications.

Table III reports statistics of our calculated trajectories. In the worst case, ($\mathscr{T}^{(0)}$ mesh, heterogeneous domain) 58% of the FE-P1 trajectories abort due to decussation. In the best case ($\mathscr{T}^{(3)}$ mesh, homogeneous domain), still 21% of the FE-P1 paths aborts. It is interesting to note that the percentage of aborted paths is larger in the heterogeneous domain than in the homogeneous one. On the contrary, only few paths abort when the RT0-P0 velocity field drives the flow. Closer inspection shows that the trajectories do not abort because of decussation, but because of non-unique velocity: by chance a mesh node was reached. Table III shows also that a large percentage of FE-P1 paths escaped the domain through the impervious boundary, and this percentage is larger when the heterogeneous domain is considered. On the contrary, all RT0-P0 paths correctly leave the domain through the boundary line segment where $p = 0$ is set, both in the homogeneous and in the heterogeneous cases.

Let us address the question of comparing the trajectory statistics exploiting two meshes, one for FE-P1, and a different one for RT0-P0, so that the ensuing FE-P1 and RT0-P0 linear system sizes are close. Table IV shows that the statistics of the particle trajectories closely resembles those of the previous meshes.

We conclude this section by noting that the results of trajectory calculations stress the importance of having continuous normal velocities across triangle edges, showing that RT0-P0 is more accurate than FE-P1 in reconstructing the constant triangle velocity vectors. However, by no means one can conclude that RT0-P0 is a conservative scheme, whereas FE-P1 is not, as shown in the LMB error calculations reported in the previous section.

## 5. CONCLUSIONS

We analyzed some properties about quantities that can be used for comparing 2D discrete velocity fields arising from the numerical solution of diffusion equations by FE-P1 (linear Galerkin) and MH (RT0-P0). We have shown that the $\mathbf{v}^{(\mathrm{FE})}$ velocity field computed by exploiting a Delaunay mesh is

DOI: 10.1002/fld

Table IV. Comparison of statistics for FE and MH trajectories. The 'Size' column reports the size of either FE or MH linear system; the remaining symbols bear the same meaning as in Table III.

| | | | Homogeneous domain | | | | Heterogeneous domain | | | |
|---|---|---|---|---|---|---|---|---|---|---|
| *M* | Size | Alg | Cor | Rex | Wex | Abr | Cor | Rex | Wex | Abr |
| 217 | 343 | RT0-P0 | 100 | 100 | 0 | 0 | 100 | 100 | 0 | 0 |
| 686 | 378 | FE-P1 | 79 | 68 | 11 | 21 | 59 | 28 | 31 | 41 |
| 868 | 1337 | RT0-P0 | 99 | 99 | 0 | 1 | 99 | 99 | 0 | 1 |
| 2744 | 1441 | FE-P1 | 84 | 79 | 5 | 16 | 73 | 34 | 39 | 27 |

conservative on properly defined *A*-cells. Our numerical experiments carried out for $f(x,y)=0$, and piecewise constant, scalar diffusion, confirmed the following noteworthy results:

- the $\mathbf{v}^{(\mathrm{MH})}$ field guarantees flux balance on both (internal) triangles and (internal) *A*-cells, whereas $\mathbf{v}^{(\mathrm{FE})}$ field fulfills flux balance on *A*-cells, but not on triangles;
- during particle tracking calculations, using the FE-P1 velocity field, we observed the following errors:
  - paths entering slow-diffusion zones;
  - velocity fields are not everywhere parallel to the impervious boundary pieces, and thus
  - wrong escapes through impervious portions of the boundary are produced;
- the trajectories calculated by RT0-P0 velocity field do not display wrong escapes and are always parallel to impervious boundaries and discontinuity interfaces.

## ACKNOWLEDGEMENTS

We would like to thank Bruce Kellogg for illuminating suggestions on theoretical questions. We thank the anonymous referees for their analysis of our manuscript and for proposing many suggestions, which improved its quality. Partial funding for this work was provided by Italian MIUR-PRIN 2004 project 'Numerical models for multiphase flow and deformation in porous media' and the University of Padova 'Progetto di Ateneo 2004'.

## REFERENCES

1. Bear J. *Dynamics of Fluids in Porous Media*. Elsevier: New York, 1972.
2. Dupont TF, Keenan PT. Superconvergence and postprocessing of fluxes from lowest order mixed methods on triangles and tetrahedra. *SIAM Journal on Scientific Computing* 1998; **19**(4):1322–1332.
3. Cordes C, Kinzelbach W. Continuous velocity fields and path lines in linear, bilinear, and trilinear finite elements. *Water Resources Research* 1992; **28**(11):2903–2911.
4. Mosé R, Siegel P, Ackerer P, Chavent G. Application of the mixed finite element approximation in a groundwater flow model: luxury or necessity? *Water Resources Research* 1994; **30**(11):3001–3012.
5. Cordes C, Kinzelbach W. Comment on 'Application of the mixed hybrid finite element approximation in a groundwater flow model: luxury or necessity?' by Mosé *et al*. *Water Resources Research* 1996; **32**(6):1905–1909.
6. Forsyth PA. A control volume finite element approach to NAPL groundwater contamination. *SIAM Journal on Scientific and Statistical Computing* 1991; **12**(5):1029–1057.
7. Putti M, Cordes C. Finite element approximation of the diffusion operator on tetrahedra. *SIAM Journal on Scientific and Statistical Computing* 1998; **19**(4):1154–1168.

8. Yeh G. On the computation of Darcy velocity and mass balance in finite elements modeling of groundwater flow. *Water Resources Research* 1981; **17**(5):1529–1534.
9. Manzini G, Putti M. Mesh locking effects in the finite volume solution of 2-d anisotropic diffusion equations. *Journal of Computational Physics* 2007; **220**:751–771. DOI: 10.1016/j.jcp.2006.05.026.
10. Meissner U. A mixed finite element model for use in potential flow problems. *International Journal for Numerical Methods in Engineering* 1972; **6**:467–473.
11. Raviart PA, Thomas JM. A mixed finite element method for second order elliptic problems. In *Mathematical Aspects of the Finite Elements Method*, Galligani I, Magenes E (eds). Lecture Notes in Mathematics, vol. 606. Springer: Berlin, New York, 1977.
12. Chavent G, Roberts JE. A unified physical presentation of mixed, mixed-hybrid finite elements and standard finite difference approximations for the determination of velocities in water flow problems. *Advances in Water Resources* 1991; **14**(6):329–348.
13. Brezzi F, Fortin M. *Mixed and Hybrid Finite Element Methods*. Springer: Berlin, 1991.
14. Hackbusch W. On first and second order box schemes. *Computing* 1989; **41**:277–296.
15. Vanselow R. Relations between FEM and FVM applied to the Poisson equation. *Computing* 1996; **57**:93–104.
16. Cordes C, Putti M. Accuracy of Galerkin finite elements for the groundwater flow equation in two and three dimensional triangulations. *International Journal for Numerical Methods in Engineering* 2001; **52**:371–387.
17. Cordes C, Putti M. Triangular mixed finite elements vs. finite differences and finite volumes in groundwater flow modeling. In *International Conference on Computational Methods in Water Resources XII*, Aldama AA, Aparicio J, Brebbia C, Pinder WGIHG (eds). Computational Mechanics and Elsevier Applied Sciences: Southampton, London, 1996; 61–68.
18. Arbogast T, Wheeler MF, Yotov I. Mixed finite elements for elliptic problems with ensor coefficients as cell-centered finite differences. *SIAM Journal on Numerical Analysis* 1997; **34**(2):828–852.
19. Arbogast T, Dawson CN, Keenan PT, Wheeler MF, Yotov I. Enhanced cell-centered finite differences elliptic equations on general geometry. *SIAM Journal on Scientific Computing* 1998; **19**(2):404–425.
20. Eymard R, Gallouët T, Herbin R. The finite volume method. In *Handbook for Numerical Analysis*, Ciarlet Ph, Lions JL (eds). North Holland: Amsterdam, 2000; 715–1022.
21. Hoteit H, Erhel J, Mosè R, Philippe B, Ackerer P. Numerical reliability for mixed methods applied to flow problems in porous media. *Computational Geosciences* 2002; **6**(2):161–194.
22. Quarteroni A, Valli A. *Numerical Approximation of Partial Differential Equations*. Springer Series in Computational Mathematics, vol. 23. Springer: Berlin, 1994.
23. Bergamaschi L, Putti M. Mixed finite elements and Newton-type linearization for the solution of Richard's equation. *International Journal for Numerical Methods in Engineering* 1999; **45**(8):1025–1046.
24. Klausen RA, Russell TF. Relationships among some locally conservative discretization methods which handle discontinuous coefficients. *Computational Geosciences* 2005; **8**:341–377. DOI: 10.1007/s10596-005-1815-9.
25. Arnold DN, Falk RS, Winther R. Finite element exterior calculus, homological techniques, and applications. *Acta Numerica* 2006; 1–155.
26. Letniowski FW. Three-dimensional Delaunay triangulations for finite element approximations to a second-order diffusion operator. *SIAM Journal on Scientific and Statistical Computing* 1992; **13**(3):765–770.
27. Kershaw DS. The incomplete Cholesky-conjugate gradient method for the iterative solution of systems of linear equations. *Journal of Computational Physics* 1978; **26**:43–65.
28. Mazzia A, Putti M. Behavior of the mixed hybrid finite element method for the solution of diffusion equations on unstructured triangulations. In *Computational Methods in Water Resources*, Miller CT, Farthing MW, Gray WG, Pinder GF (eds), vol. 1. Elsevier: Amsterdam, 2004; 1053–1066.
29. Marini LD. An inexpensive method for the evaluation of the solution of the lowest order Raviart–Thomas mixed method. *SIAM Journal on Numerical Analysis* 1985; **22**(3):493–496.
30. Kellogg RB. On elliptic interface problems. *Personal Communication* 2006.
31. Risler JJ. *Mathematical Methods for CAD*. Cambridge University Press: Cambridge, MA, 1992.
32. Bank RE, Rose DJ. Some error estimates for the box method. *SIAM Journal on Numerical Analysis* 1987; **24**(4):777–787.
33. Mazzia A. An analysis of monotonicity conditions in the mixed hybrid finite element method on unstructured triangulations. *International Journal for Numerical Methods in Engineering*, 2008; DOI: 10.1002/nme.2330.
34. The MathWorks Inc. *MATLAB. Complete Documentation*. The MathWorks Inc., Natick, MA, 2008. Available from: http//www.mathworks.com/access/helpdesk/help/techdoc/matlab.html (21 March 2008).
35. Johnson C. *Numerical Solutions of Partial Differential Equations by the Finite Element Method*. Cambridge University Press: New York, 1987.